Supplementary Information

Steam-promoted Symmetry optimizations on Perovskite Electrodes for Protonic Ceramic Cells

Feng Zhu[a], Mingyang Hou[a], Zhiwei Du[a], Fan He[a], Yangsen Xu[a], Kang Xu[a], Hui Gao[a], Ying Liu[b] and Yu Chen[a,*]

[a]School of Environment and Energy, South China University of Technology, Guangzhou 510006, China

[b]Research Institute of Renewable Energy and Advanced Materials, Zijin Mining Group Co., Ltd., Xiamen, Fujian 361101, China

*Corresponding author:

Yu Chen. E-mail: eschenyu@scut.edu.cn

Materials and Methods

Preparation of powders

$Pr_{0.5}Ba_{1/6}Sr_{1/6}Ca_{1/6}CoO_{3-\delta}$ (PBSCC) powder was prepared by a sol-gel complexing method. A stoichiometric amount of metal nitrates was dissolved in deionized water. Complexing agents of citric acid (CA) and ethylenediaminetetraacetic acid (EDTA) were then added to the mixed solution with the molar ratio of metal ions: CA: EDTA = 1: 2: 1. $NH_3 \cdot H_2O$ was used to adjust the pH value of the solution to ~7. After evaporating the water at 120 ^oC, the formed gel was moved to an oven and heated at 300 ^oC for 5 h to ensure complete combustion. Finally, the obtained ash was calcined at 1000 ^oC for 5 h to obtain PBSCC powder. The NiO powder was commercially available from H2-BANK. The $BaZr_{0.1}Ce_{0.7}Y_{0.1}Yb_{0.1}O_{3-\delta}$ (BZCYYb) electrolyte powder was prepared by a solid-state reaction method. Specifically, stochiometric amounts of $BaCO_3$, ZrO_2, CeO_2, Y_2O_3, and Yb_2O_3 powders were mixed in ethanol and ball-milled at 400 rpm for 4 h. After completely dried, the mixture was then uniaxially pressed into a pellet at 10 MPa and sintered at 1100 ^oC for 12 h two times.

Fabrication of symmetrical cells

Dense BZCYYb electrolyte pellets were fabricated by uniaxially pressing as-synthesized BZCYYb powder (mixed with 1% polyvinyl butyral) and followed by sintering at 1450 ^oC for 5 h in air. Symmetrical cells with a configuration of PBSCC|BZCYYb|PBSCC were prepared by painting the PBSCC oxygen electrode slurry onto both sides of the BZCYYb pellets (with an effective area of 0.2826 cm^2) followed by calcining at 1000 ^oC for 2 h. The PBSCC electrode slurry was prepared by mixing PBSCC powder, terpineol, and ethyl cellulose with a weight ratio of 100: 76: 4.

Fabrication of tubular single cells

The tubular NiO-BZCYYb fuel electrode-supported single cells were fabricated by a phase inversion technique. Polyethersulfone (PESf) as a polymer binder and N-Methyl pyrrolidone (NMP) as a solvent were used to prepare the polymer solution. Deionized

water was chosen as the external coagulant, which functioned as the non-solvent to trigger the phase separation process. The fuel electrode slurry was obtained by the ball-milling of NiO and BZCYYb powders in the polymer solution for 48 h. Specifically, 21.6 g BZCYYb, 32.4 g NiO, 6.75 g graphite, 0.75 g polyvinyl pyrrolidone (PVP), 3.0 g PESf, and 18.0 g NMP were mixed. The dry glass rod (with a diameter of 4 mm) was first immersed in the fuel electrode slurry and then soaked in deionized water for 10 h. Phase inversion took place as mass exchange between the slurry and water. The fuel electrode slurry on glass rods eventually solidified to form round tubes. After peeling off from the glass rods and drying overnight in ambient air, the raw tubes were heated at 1000 ^{o}C for 2 h to obtain the fuel electrode substrate. Before the fabrication of fuel electrode functional layer and electrolyte layer, wax was applied to seal one end of the tube, avoiding the contact between the inner surface of the tube and the slurries. Then, the fuel electrode substrate was successively immersed into the slurries of the fuel electrode functional layer and electrolyte layer. After removing the wax, the tube with the functional layer and electrolyte layer was sintered at 1450 ^{o}C for 5 h to form a fuel electrode-supported tubular half-cell. Finally, the PBSCC oxygen electrode slurry was painted on the outer surface (the dense BZCYYb electrolyte surface) of the tubes.

Material characterizations and electrochemical measurements

The X-ray diffraction (XRD) was performed to detect the phase structures of powders. High-resolution images of lattice fringes and elemental distribution were performed using a transmission electron microscope (TEM, Thermo Talos F200X G2) equipped with an energy-dispersive X-ray spectrometer (EDX) system. The microstructure and morphology of the cells were examined by a cold field emission scanning electron microscopy (SEM, Hitachi SU8010). The elemental valence states on the surface of samples were analyzed by an X-ray photoelectron spectrometer (XPS, Thermo Scientific K-Alpha). The as-synthesized PBSCC powder was mixed with 1% polyvinyl butyral and then pressed into a rectangular bar. The green bar was then sintered at 1200 ^{o}C for 10 h in the air to densify the bar for the measurements of electrical conductivity relaxation (ECR). The ECR technique was used for the D_{chem} and k_{chem} of electrode

material, tested by a digital source meter (Keithley, 2450). The thermodynamic weight loss of samples from room temperature (RT) to 800 ^{o}C in the air with a heating rate of 10 ^{o}C min^{-1} was examined by thermogravimetric (TG, Netzsch TG 209 F3) analysis.

The symmetrical cells were tested under open-circuit voltage (OCV) conditions in dry and wet air (3% H_2O). Different oxygen partial pressure was achieved by supplying different volume of pure O_2 and pure N_2. For the test of fuel cell (FC) mode, 30 mL min^{-1} humidified H_2 (3% H_2O) was supplied to the fuel electrode as fuel and ambient air in the oxygen electrode as oxidant. For the test of electrolysis (EL) mode and reversible mode, 30 mL min^{-1} humidified H_2 (3% H_2O) was supplied to the fuel electrode, and the oxygen electrode was exposed to 100 mL min^{-1} wet air (3% H_2O). Faradic efficiencies (FE) were measured based on the ratio of the experimental and theoretical amount of H_2 produced at different steam concentrations and different current densities. The fuel electrode was fed with 45 mL min^{-1} 10%H_2-90%Ar and the oxygen electrode was fed with 100 mL min^{-1} humidified air. Gas chromatography (GC, GC-7820) was employed to detect the H_2 concentrations in fuel electrode in real time *via* an automatic sampling valve. The Electrochemical impedance spectroscopy (EIS) and current-voltage (*I-V*) curves were measured by an electrochemical workstation (PARSTAT MC200).

Supplementary Note 1

Shown in **Fig. S1** are the SEM images of as-synthesized PBSCC powders after being calcined at 1000 °C for 5 h. According to **Fig. S1a**, the average particle size of the as-synthesized PBSCC powders was determined to be ~432 nm. In particular, some grains showed a relatively smooth surface (**Fig. S1b**), while many small particles appeared on the surface of others (**Fig. S1c**). This phenomenon was observed many times in PBSCC powders (**Fig. S1d** and **e**). Therefore, we speculate that these small particles may be grains that are still in the growth stage.

Supplementary Note 2

The fuel electrode-supported layer prepared by the phase conversion method usually forms finger-like pores, which are conducive to the rapid transport of fuel gas, thus reducing the concentration polarization and enhancing cell performance. The effects of the content of solvent NMP and polymer binder PESf in the casting slurry on the microstructure of the fuel electrode-supported layer were systematically investigated by Ren et al.[1] The results indicated that different amounts of NMP and PESf significantly affect the microstructure, gas permeation, and mechanical strength of the fuel electrode substrate by regulating the viscosity of the casting slurry. For example, increasing the NMP amount favors the formation of finger-like pores, whereas excessive NMP would inhibit the formation of finger-like pores. Similarly, too high PESf concentration would result in the disappearance of finger-like pores. Compared to our previous work[2], we adjusted the composition of the casting slurry in this work, which may be the main reason for the difference in the microstructure of the fuel electrode substrate. In addition, the microstructures of the fuel electrode of the cell after the long-term durability test for over 500 h were examined by SEM. As shown in **Fig. S10**, straight finger-like pores with a few dozen micrometers in length can be observed between the fuel electrode-supported layer and electrolyte layer.

Supplementary Note 3

The relatively low FE is likely ascribed to the p-type electronic leakage across the BZCYYb electrolyte.[3-5] Proton-conducting electrolytes in the cerate-zirconate family are generally not pure proton conductors. Depending on the temperature and chemical potential conditions, these electrolytes possess mixed charge carriers, including protons ($^{OH_O^{\bullet}}$), oxygen vacancies ($^{V_O^{\bullet\bullet}}$), electrons (e^-) and/or electron holes ($^{h^{\bullet}}$).[4] Under moist conditions, protons are formed by the incorporation of water into oxygen vacancies *via* the hydration reaction: $^{H_2O(g) + V_O^{\bullet\bullet} + O_O^{\times} \leftrightarrow 2OH_O^{\bullet}}$. However, electron holes are produced by a parasitic oxidation reaction ($^{\frac{1}{2}O_2 + V_O^{\bullet\bullet} \leftrightarrow 2h^{\bullet} + O_O^{\times}}$) that occurs in an oxidizing atmosphere *via* the incorporation of molecular oxygen into oxygen vacancies.[6,7] Both the beneficial hydration reaction that promotes proton formation and parasitic oxidation reactions that produce detrimental electron holes, occur at the interface between oxygen electrode and the electrolyte.[8] According to Le Chatelier's principle, high steam concentrations facilitate the hydration reaction and inhibit the formation of electron holes, thus increasing the FE. As shown in **Fig. S13a**, when the water concentration was increased from 5% to 50% at -0.5 A cm^{-2}, the FE was increased from ~54.3% to ~83.6%. Moreover, at high current densities, the relatively slow mass transport within the electrode may significantly affect the gas phase composition at the interface between the electrode and electrolyte.[8] Due to the continuous consumption of steam in EL mode, the local water partial pressure decreases and the oxygen partial pressure increases, which is conducive to the parasitic oxidation reaction.[4,9] Therefore, the electron holes formed by the parasitic oxidation reaction lead to the reduction of FE. As shown in **Fig. S13b**, when the electrolysis current density was increased from -0.5 A cm^{-2} to -0.75 A cm^{-2}, the FE decreased from ~83.6% to 78.7%. In addition, since the FE test is based on laboratory-scale tubular cells, gas leakage caused by improper sealing may also significantly affect the hydrogen production rate.

Supplementary Note 4

The dependence of phase composition in varying steam concentrations and time has been analyzed. During *in situ* high-temperature XRD (HT-XRD) testing, the PBSCC sample was exposed to 30% H_2O humidified air for 4 h at 600 °C. As shown in **Fig. S15**, the content of the cubic phase increases with an increase in duration. Furthermore, the PBSCC samples were also treated in varying steam concentrations (such as 3%, 10%, and 20%) at 600 °C for 1 h. Then the samples were taken out from the high-temperature furnace at about 200 °C and sealed to keep the steam in the lattices (steam was continuously supplied to the sample chamber throughout the process). As shown in **Fig. S16**, the content of the cubic phase increases slightly with the increase of steam concentrations. It should be noted that, compared with the results from in situ tests, the results (such as the steam concentrations retained in the bulk phase of the samples) obtained by this *ex situ* treatment are inevitably different from the actual situations to some extent.

Supplementary Note 5

The PBSCC sample was first treated in 30% H_2O for 100 h at 600 °C to complete the phase transition and hydration process ($H_2O(g) + V_O^{\bullet\bullet} + O_O^{\times} \leftrightarrow 2OH_O^{\bullet}$). Specifically, the sample was taken out from the high-temperature furnace at 200 °C and sealed to keep the steam in the lattices (steam was continuously supplied to the sample chamber throughout the process). At the elevated temperatures from RT to 800 °C in air, the weight loss of the as-synthesized PBSCC sample is attributed to the release of oxygen from the lattice ($O_O^{\times}$), while the weight loss of hydrated PBSCC sample is composed of the desorption of oxygen and H_2O (by dehydration in which hydrated protons ($OH_O^{\bullet}$) dissociate from oxygen vacancies). In addition, it is noted that a weight increase occurring at 200~300 °C (**Fig. 4h**) is likely attributed to the oxidization of Co from low to high valence states, which has been observed several times in cobalt-containing perovskite materials.[10-13] In this interval, the stronger weight variation of the PBSCC before hydration may be due to the higher Co^{3+} content (**Fig. 4g** and **S19**).

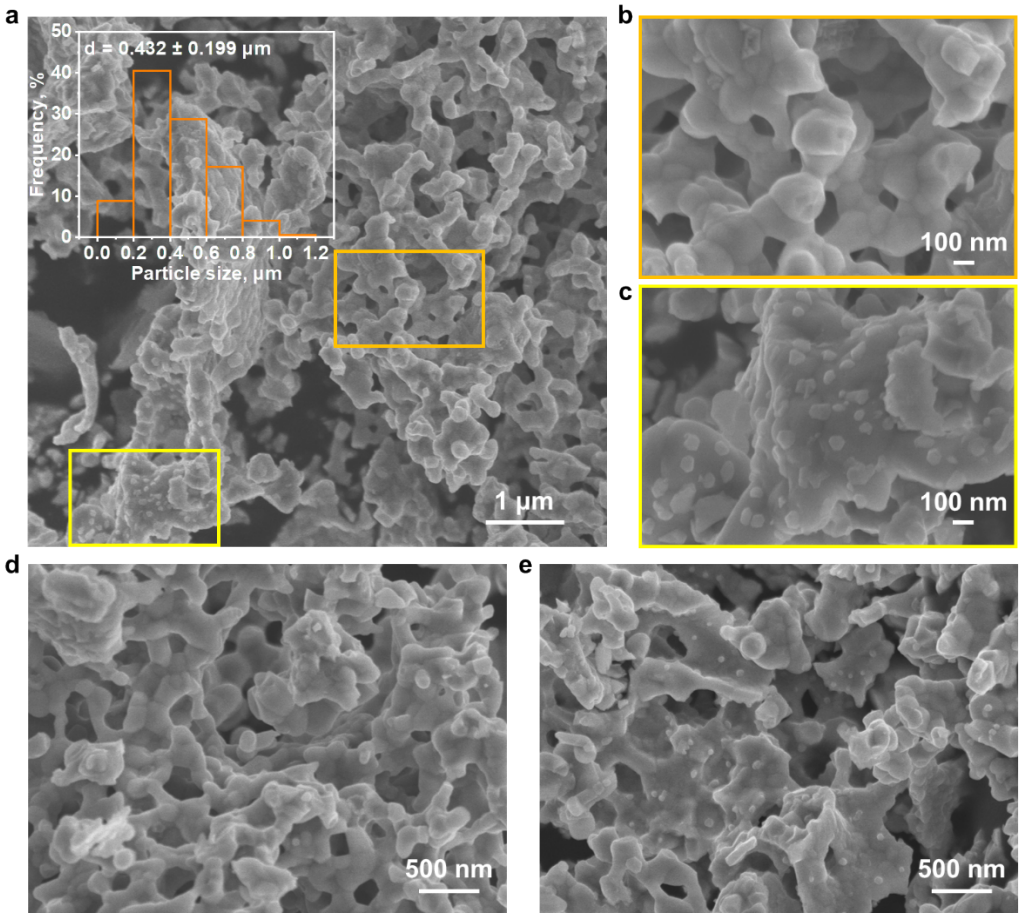

Figure S1. (a-e) SEM images of as-synthesized PBSCC powders after being calcined at 1000 ^{o}C for 5 h. Some nanoparticles (c and e) were observed on the surface of PBSCC powders.

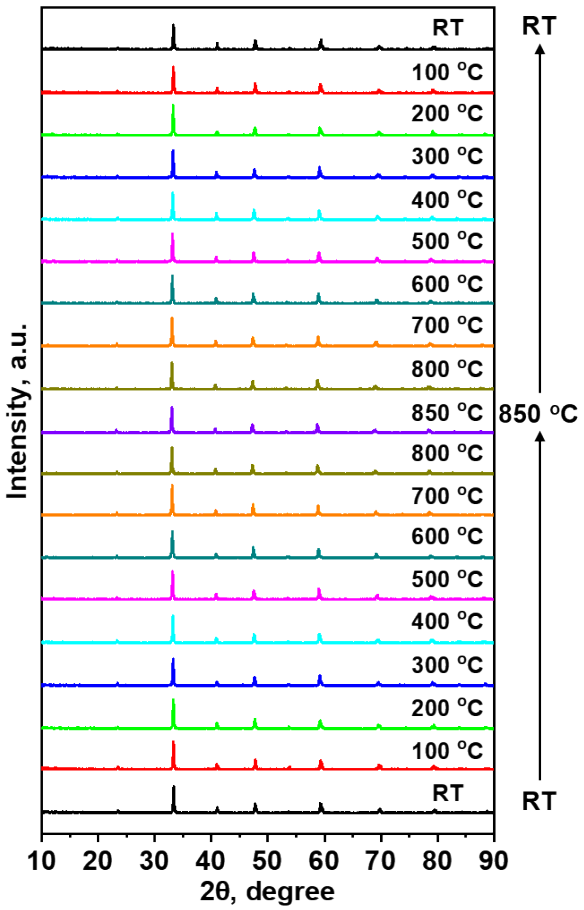

Figure S2. The *in situ* HT-XRD patterns of as-synthesized PBSCC sample from RT to 850 °C in ambient air.

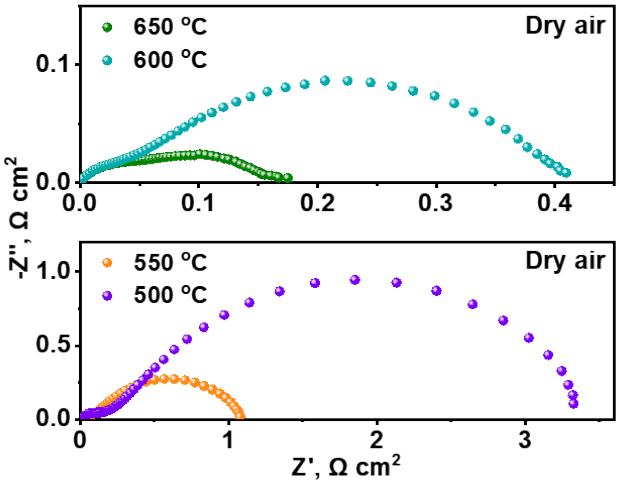

Figure S3. Typical EIS of BZCYYb-based symmetrical cells with a PBSCC electrode tested at dry air under OCV conditions.

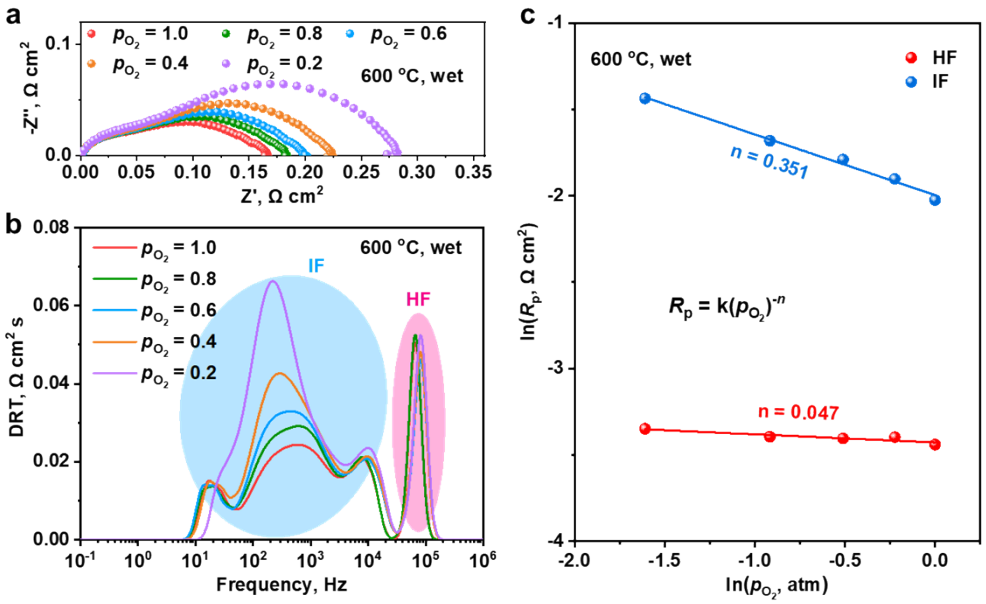

Figure S4. (a) Typical EIS and (b) corresponding DRT plots of PBSCC as a function of p_{O2} in wet conditions. (c) Dependence of each R_p of PBSCC electrode as a function of p_{O2} at 600 °C in wet conditions.

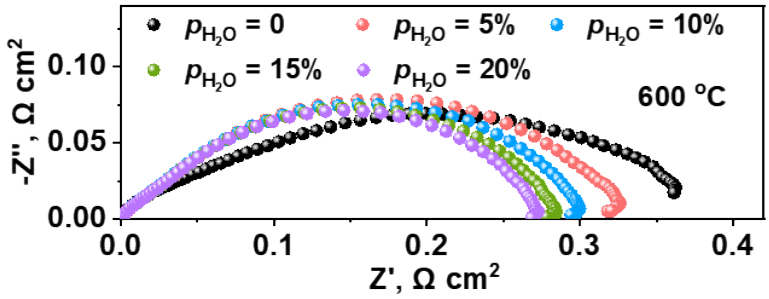

Figure S5. Typical EIS of symmetrical cell with PBSCC electrode as a function of p_{H2O} at 600 °C.

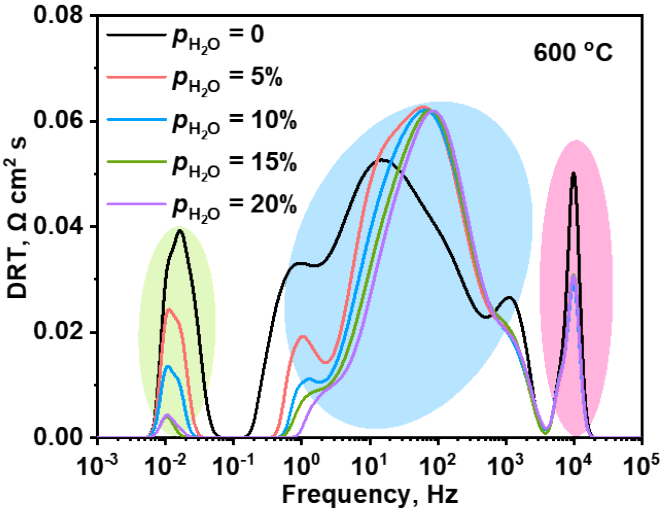

Figure S6. The corresponding DRT plots of symmetrical cell with PBSCC electrode as a function of p_{H2O} at 600 °C.

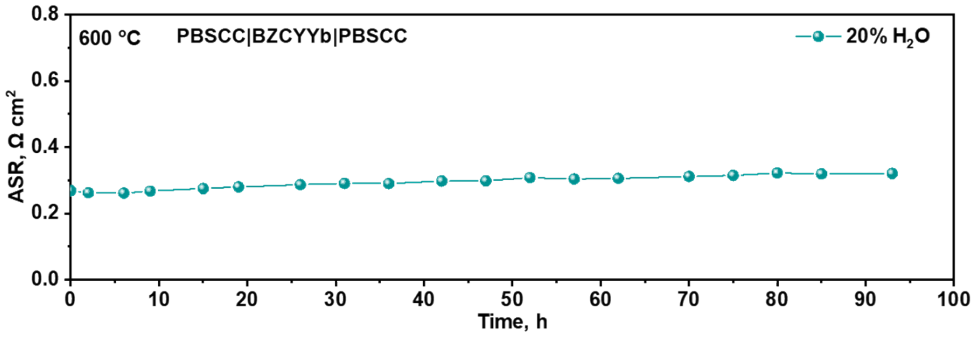

Figure S7. Short-term area-specific resistance (ASR) durability of PBSCC electrode in wet air (20% H_2O) under OCV conditions at 600 °C.

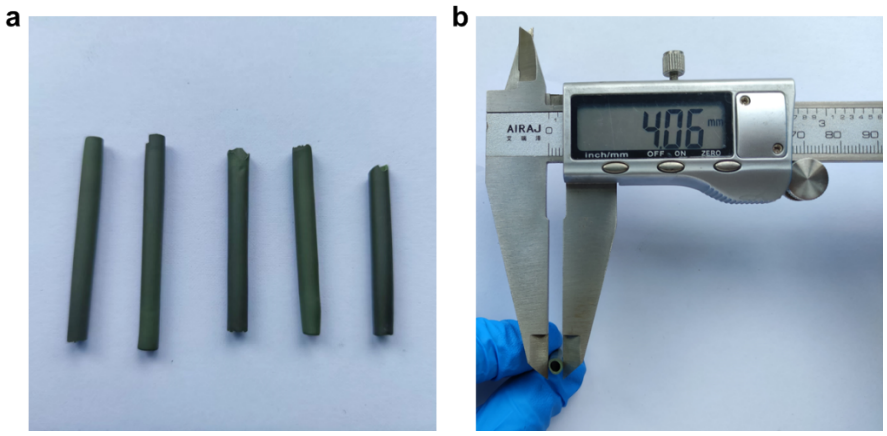

Figure S8. (a) Image of the fuel electrode-supported tubular half-cells. (b) An image of the tubular cell with a diameter of about 4 mm.

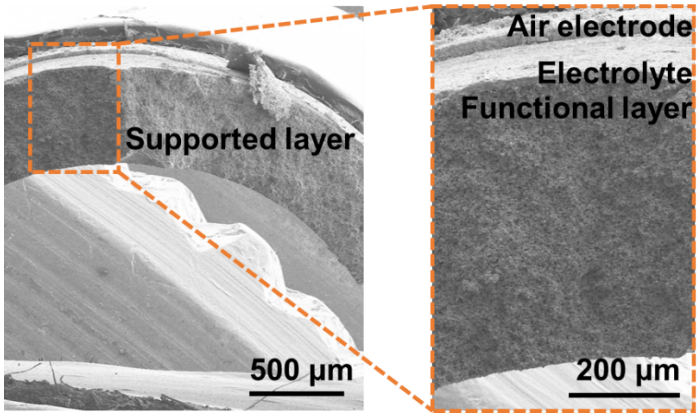

Figure S9. SEM images of the fuel electrode-supported tubular cell with PBSCC oxygen electrode after the long-term durability test for over 500 h, consisting of a porous Ni-BZCYYb fuel electrode-supported layer, a porous Ni-BZCYYb functional layer, a thin BZCYYb electrolyte layer, and a porous PBSCC oxygen electrode.

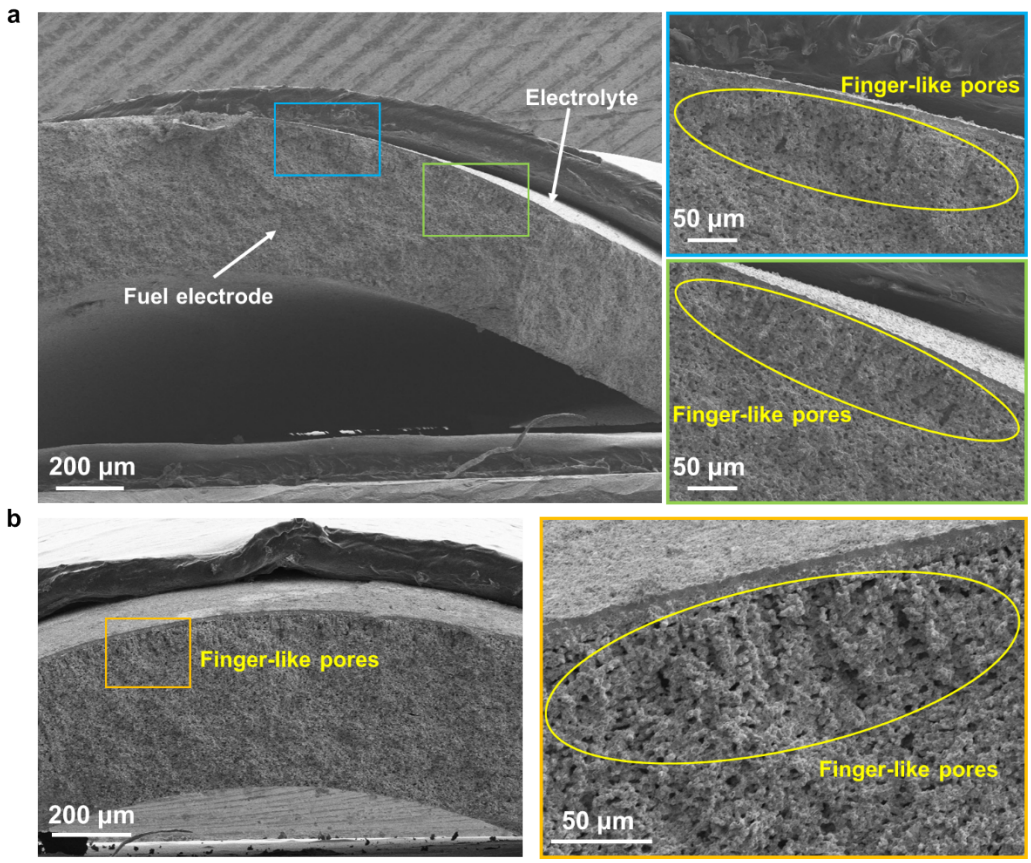

Figure S10. (a, b) SEM images of the fuel electrode-supported tubular cell after the long-term durability test for over 500 h. Straight finger-like pores between the fuel electrode-supported layer and electrolyte layer can be observed in the enlarged SEM images.

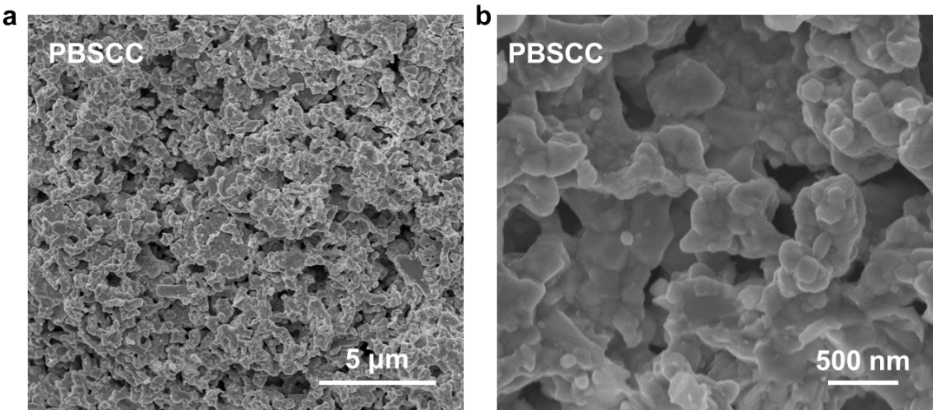

Figure S11. (a, b) High-magnification SEM image of the PBSCC oxygen electrode after the long-term durability test.

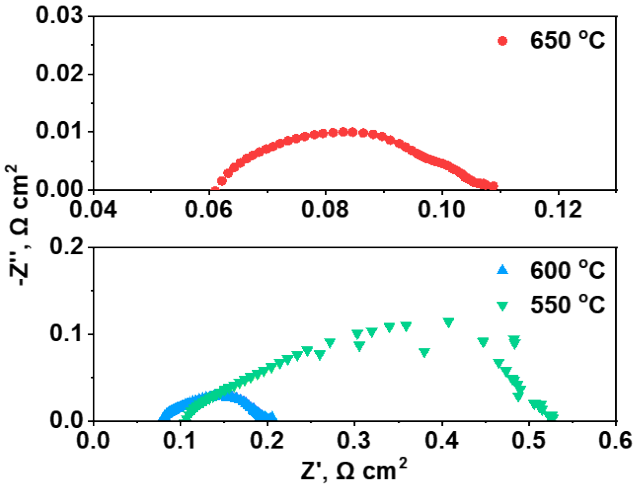

Figure S12. EIS curves of an R-PCC with PBSCC oxygen electrode measured at 650-550 °C under OCV conditions.

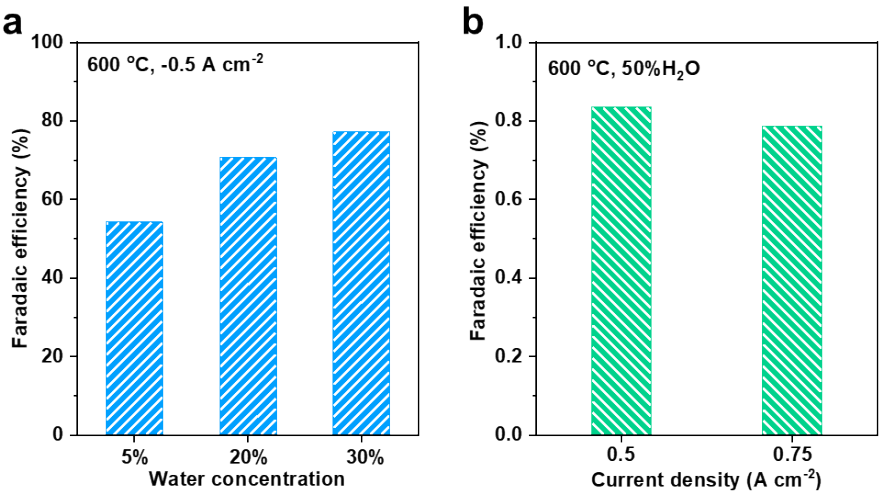

Figure S13. Faradaic efficiencies of tubular R-PCCs for producing hydrogen at (a) different H_2O concentrations in air, and (b) different electrolysis current densities with 50% H_2O humidified air at 600 °C.

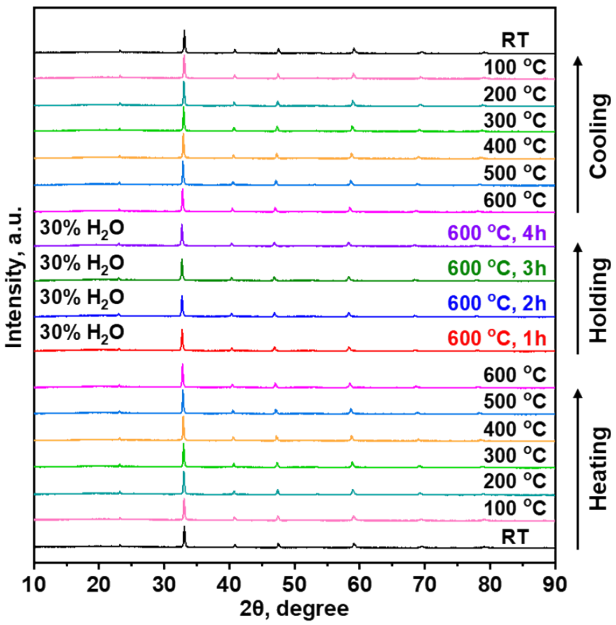

Figure S14. The *in situ* HT-XRD patterns of the PBSCC sample from RT to 600 °C in 30% H_2O humidified air.

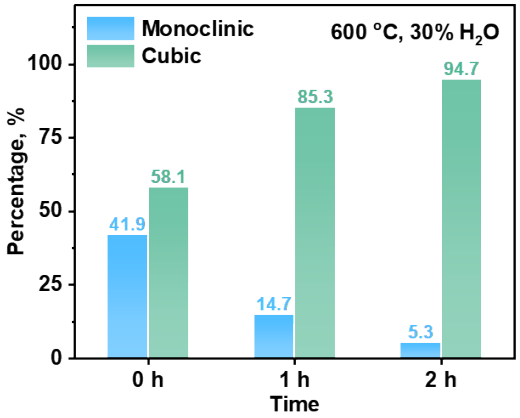

Figure S15. The refined results of the content of the two phases during the steam injection at 600 °C.

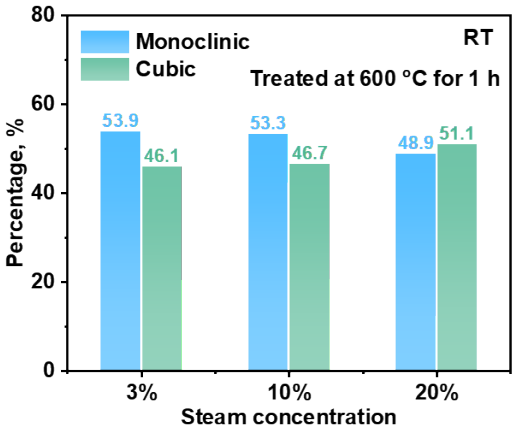

Figure S16. The dependence of phase composition in varying steam concentrations. The data were obtained through refining the XRD patterns tested at RT.

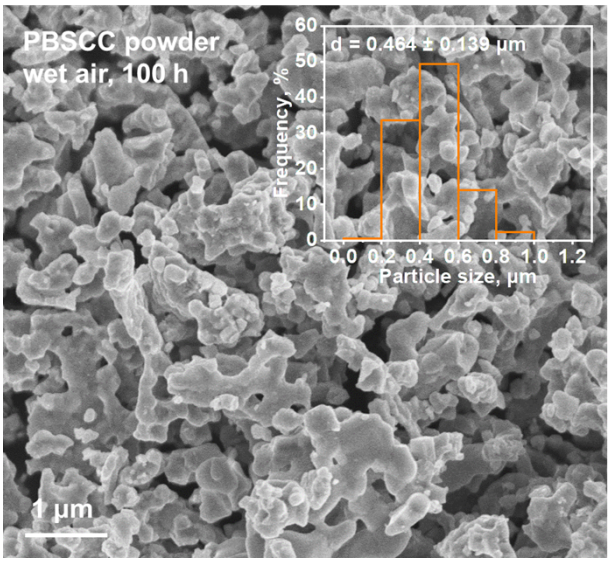

Figure S17. SEM images of PBSCC powders after being treated with 30% H_2O at 600 °C for 100 h. The inset is the corresponding size distribution.

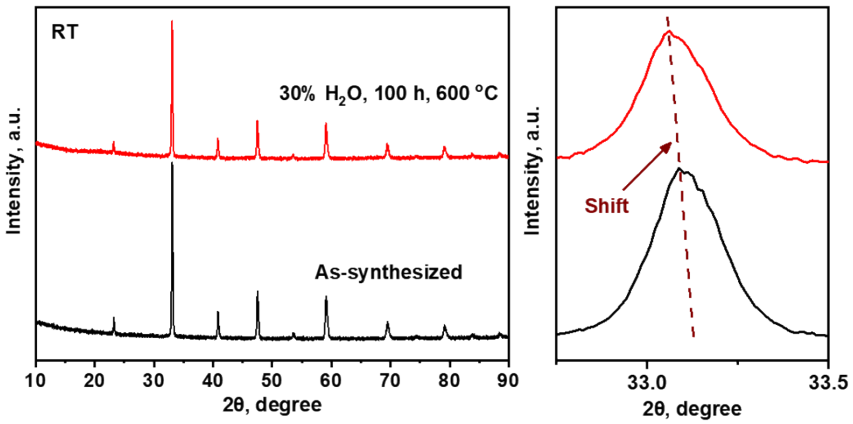

Figure S18. RT XRD patterns of the PBSCC powder before and after treatment in wet air (30% H_2O) for 100 h at 600 °C.

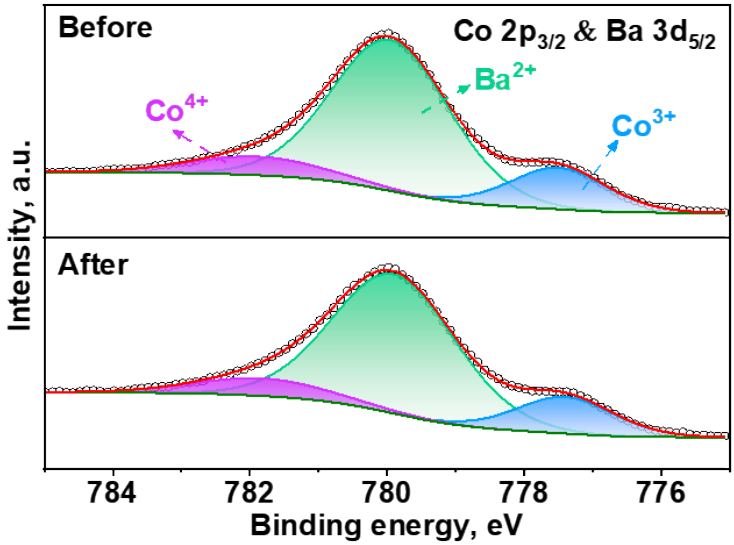

Figure S19. XPS spectra of Ba $3d_{5/2}$ and Co $2p_{3/2}$ for PBSCC sample before and after being treated in wet air (30% H_2O) for 100 h at 600 °C.

Table S1. Refinement paraments of the as-synthesized PBSCC at RT and the steam-contained PBSCC after steam injection for 4 h at 600 °C.

Sample	R_p (%)	R_{wp} (%)	χ^2	Space group	a (Å)	b (Å)	c (Å)	α	β	γ
PBSCC-before	2.53	3.17	1.160	P21/n	5.396502	5.410897	7.659056	90.000	90.197	90.000
PBSCC-after	3.74	4.69	1.643	$Pm\bar{3}m$	3.883324	3.883324	3.883324	90.000	90.000	90.000

Table S2. Peak power densities comparison (FC mode) of our tubular R-PCC and other high-performance fuel electrode-supported single cells reported recently with similar configuration.

Oxygen electrode	Electrolyte (thickness, μm)	Fuel electrode	Cell structure	Temp. (°C)	PPD (W cm^{-2})	Authors, Year
$BaCo_{0.4}Fe_{0.4}Zr_{0.1}Y_{0.1}O_{3-\delta}$ (BCFZY)	BZCYYb+1wt% NiO (15 μm)	Ni-BZCYYb	Planar	600 550	0.65 0.52	Duan et al., 2015[14]
$PrNi_{0.5}Co_{0.5}O_{3-\delta}$ (PNC) nano-fiber	BZCYYb4411[a] (10 μm)	Ni-BZCYYb4411	Planar	600 550	0.61 0.44	Ding et al., 2020[15]
$Gd_{0.3}Ca_{2.7}Co_{3.82}Cu_{0.18}O_{9-\delta}$ (GCCCO)-BZCYYb	BZCYYb (15 μm)	Ni-BZCYYb	Planar	700 650 600 550 500	2.05 1.60 1.16 0.77 0.48	Saqib et al., 2021[16]
$Na_{0.15}Ca_{2.85}Co_4O_{9-\delta}$ (NCC)	BZCYYb (~7 μm)	Ni-BZCYYb	Planar	700 650 600 550 500	3.42 2.47 1.70 1.10 0.48	Park et al., 2022[17]
$NdBa_{0.5}Sr_{0.5}Co_{1.5}Fe_{0.5}O_{5+\delta}$ (NBSCF)	BZCYYb (14.7 μm)	Ni-BZCYYb	Planar	700 650 600	1.37 1.05 0.69	Kim et al., 2014[18]
$Ba_{0.95}(Co_{0.4}Fe_{0.4}Zr_{0.1}Y_{0.1})_{0.95}Ni_{0.05}O_{3-\delta}$ (BCFZYN)	BZCYYb (~12 μm)	Ni-BZCYYb	Planar	650 600 550	1.04 0.71 0.54	Liang et al., 2022[19]
$PrBaCo_{1.6}Fe_{0.2}Nb_{0.2}O_{5+\delta}$ (PBCFN)	BZCYYb (~10 μm)	Ni-BZCYYb	Planar	700 650 600	1.46 1.06 0.72	Xu et al., 2022[20]

$Ba_{0.9}Co_{0.7}Fe_{0.2}Nb_{0.1}O_{3-\delta}$ (BCFN)	BZCYYb (~10 μm)	Ni-BZCYYb	Planar	650 600 550	1.70 1.20 0.80	Pei et al., 2022[21]
$PrBa_{0.5}Sr_{0.5}Co_{1.5}Fe_{0.5}O_{5+\delta}$ (PBSCF) with a PLD[b] layer	BZCYYb4411 (~15 μm)	Ni-BZCYYb4411	Planar	600 550 500	1.10 0.80 0.55	Choi et al., 2018[22]
$Ba_{0.62}Sr_{0.38}CoO_{3-\delta}$-$Pr_{1.44}Ba_{0.11}Sr_{0.45}Co_{1.32}Fe_{0.68}O_{6-\delta}$ (BSC-PBSCF)	BZCYYb+1wt% NiO (~3 μm)	Ni-BZCYYb	Planar	600 550	1.64 1.21	Liu et al., 2023[23]
$BaCo_{0.8}Ta_{0.2}O_{3-\delta}$ (BCT20) with a PLD layer	BZCYYb4411 (10 μm)	Ni-BZCYYb4411	Planar	650 600 550 500	2.26 1.64 1.14 0.76	Kim et al., 2023[24]
BCT20 without PLD layer	BZCYYb4411 (10 μm)	Ni-BZCYYb4411	Planar	650 600 550 500	1.83 1.35 0.90 0.52	Kim et al., 2023[24]
$Pr_{0.2}Ba_{0.2}Sr_{0.2}La_{0.2}Ca_{0.2}CoO_{3-\delta}$ (PBSLCC)	BZCYYb (~10 μm)	Ni-BZCYYb	Planar	650 600 550	1.51 1.16 0.72	He et al., 2023[25]
$BaSc_{0.1}Ta_{0.1}Co_{0.8}O_{3-\delta}$ (BSTC) with a PLD layer	BZCYYb4411 (~6.5 μm)	Ni-BZCYYb4411	Planar	650 600 550	3.15 2.25 1.46	Kim et al., 2024[26]
$BaSc_{0.1}Ta_{0.1}Co_{0.8}O_{3-\delta}$ (BSTC) with a PLD layer	BZCYYb4411 (~6.5 μm)	Ni-BZCYYb4411	Planar	650 600 550	2.41 1.70 1.15	Kim et al., 2024[26]
PBSCF without a PLD layer	BZCYYb4411 (~8 μm)	Ni-BZCYYb4411	Planar	650 600 550	~1.20 ~0.90 ~0.66	Choi et al., 2024[27]

$PrBa_{0.5}Sr_{0.5}Co_{1.5}Fe_{0.5}O_{5+\delta}$ (PBSCF)	BZCYYb (8 μm)	Ni-BZCYYb (with a Fe catalytic layer)	Tubular	700 650	1.51 1.16	Pan et al., 2022[2]
$La_{0.6}Sr_{0.4}Co_{0.2}Fe_{0.8}O_{3-\delta}$ (LSCF)	BZCYYb (12 μm)	Ni-BZCYYb	Tubular	700 650 600	0.90 0.72 0.59	Dong et al., 2020[28]
PBSCC	BZCYYb (~6 μm)	Ni-BZCYYb	Tubular	650 600 550	2.44 1.40 0.80	This work

a) BZCYYb4411: $BaZr_{0.4}Ce_{0.4}Y_{0.1}Yb_{0.1}O_{3-\delta}$. b) PLD: pulsed laser deposition.

Table S3. Water splitting Performance comparison (EL mode) of our tubular R-PCC and other high-performance fuel electrode-supported single cells reported recently with similar configuration.

Oxygen electrode	Electrolyte (thickness, μm)	Fuel electrode	Cell structure	Temp. (°C)	Current density @1.3 V (A cm^{-2})	Fuel condition (Fuel electrode: F, Oxygen electrode: O)	Authors, Year
$PrBa_{0.9}Co_{1.96}Nb_{0.04}O_{5+\delta}$ (PBCN)	BZCYYb (16.1 μm)	Ni-BCZYYb	Planar	650 600 550	-2.75 -1.73 -1.07	F: 97% H_2, 3% H_2O O: 3% H_2O, 97% air	Zhang et al., 2021[29]
PBCFN	BZCYYb (~10 μm)	Ni-BCZYYb	Planar	700 650 600	-3.85 -2.15 -1.04	F: 97% H_2, 3% H_2O O: 3% H_2O, 97% air	Xu et al., 2022[20]
NBSCF-BZCYYb	BZCYYb (20 μm)	Ni-BCZYYb	Planar	700 650 600 550	-2.41 -1.62 -0.75 -0.42	F: 90% H_2, 10% H_2O O: 10% H_2O, 90% air	Kim et al., 2018[30]
$Gd_xCo_yO_{3-\delta}$-$Ba_{0.8}Gd_{0.8-x}Pr_{0.4}Co_{2-y}O_{5+\delta}$ (GCO-BGPC)	BZCYYb (~10 μm)	Ni-BCZYYb	Planar	700 650 600	-3.49 -2.34 -1.32	F: 97% H_2, 3% H_2O O: 3% H_2O, 97% air	Zhu et al., 2022[31]
$PrBa_{0.9}Cs_{0.1}Co_2O_{5+\delta}$ (PBCsC)	BZCYYb (~8 μm)	Ni-BCZYYb	Planar	650 600 550 500	-2.85 -1.48 -0.71 -0.31	F: 97% H_2, 3% H_2O O: 3% H_2O, 97% air	Xu et al., 2023[32]
PNC nano-fiber	BZCYYb4411 (10 μm)	Ni-BCZYYb4411	Planar	600 550	-1.18 -0.80	F: dry 10% H_2 O: ~10% H_2O	Ding et al., 2020[15]
PBSCF with a PLD layer	BZCYYb4411 (~15 μm)	Ni-BCZYYb4411	Planar	650 600 550	-2.90 -1.92 -1.00	F: 97% H_2, 3% H_2O O: 3% H_2O, 97% air	Choi et al., 2019[3]
$PrBa_{0.8}Ca_{0.2}Co_2O_{5+\delta}$-$BaCoO_{3-\delta}$ (PBCC-BCO)	BZCYYb (~10 μm)	Ni-BCZYYb	Planar	650	-2.52	F: 97% H_2, 3% H_2O O: 3% H_2O, 97% air	Zhou et al., 2021[5]

				600	-1.51	
				550	-0.69	
GCCCO-BZCYYb	BZCYYb (15 μm)	Ni-BCZYYb	Planar	700 650 600 550 500	-4.30 -3.00 -2.13 -1.25 -0.75	F: 10% H_2, 90% N_2 O: 20% H_2O, 80% air	Saqib et al., 2021[16]
BCT20-BZCYYb	BZCYYb4411 (10 μm)	Ni-BCZYYb4411	Planar	650 600 550	-2.70 -1.99 -1.10	F: 97% H_2, 3% H_2O O: 3% H_2O, 97% air	Kim et al., 2023[24]
BSTC with a PLD layer	BZCYYb4411 (~6.5 μm)	Ni-BCZYYb4411	Planar	650 600 550	-4.21 -2.88 -1.49	F: 97% H_2, 3% H_2O O: 3% H_2O, 97% air	Kim et al., 2024[26]
BSTC with a PLD layer	BZCYYb4411 (~6.5 μm)	Ni-BCZYYb4411	Planar	650 600 550	-3.26 -2.33 -1.22	F: 97% H_2, 3% H_2O O: 3% H_2O, 97% air	Kim et al., 2024[26]
PBSCF with a PLD layer	BZCYYb4411 (~8 μm)	Ni-BCZYYb4411	Planar	650 600 550	-3.20 -2.25 -1.50	F: 20% H_2, 80% Ar O: 20% H_2O, 80% air	Choi et al., 2024[27]
PBSCF without PLD layer	BZCYYb4411 (~8 μm)	Ni-BCZYYb4411	Planar	650 600 550	-1.48 -0.90 -0.50	F: 20% H_2, 80% Ar O: 20% H_2O, 80% air	Choi et al., 2024[27]
PBSCF	BZCYYb (~6 μm)	Ni-BCZYYb	Tubular	700 650 600	-4.67 -3.03 -1.59	F: 97% H_2, 3% H_2O O: 3% H_2O, 97% air	Hou et al., 2023[33]
$Pr_2NiO_{3.9+\delta}F_{0.1}$ (PNOF)	BZCYYb (~20 μm)	Ni-BCZYYb	Tubular	650	-2.00	F: 97% H_2, 3% H_2O O: 50% H_2O, 50% air	Li et al., 2021[34]
PBSCC	BZCYYb (~6 μm)	Ni-BCZYYb	Tubular	650 600 550	-3.79 -2.19 -0.95	F: 97% H_2, 3% H_2O O: 3% H_2O, 97% air	This work

References

1. C. Ren, T. Liu, Y. Mao, P. Maturavongsadit, J. A. Luckanagul, Q. Wang and F. Chen, *Electrochim. Acta*, 2014, **149**, 159-166.
2. Y. Pan, H. Zhang, K. Xu, Y. Zhou, B. Zhao, W. Yuan, K. Sasaki, Y. Choi, Y. Chen and M. Liu, *Appl. Catal., B: Environ.*, 2022, **306**, 121071.
3. S. Choi, T. C. Davenport and S. M. Haile, *Energy Environ. Sci.*, 2019, **12**, 206-215.
4. C. Duan, R. Kee, H. Zhu, N. Sullivan, L. Zhu, L. Bian, D. Jennings and R. O'Hayre, *Nat. Energy*, 2019, **4**, 230-240.
5. Y. Zhou, E. Liu, Y. Chen, Y. Liu, L. Zhang, W. Zhang, Z. Luo, N. Kane, B. Zhao, L. Soule, Y. Niu, Y. Ding, H. Ding, D. Ding and M. Liu, *ACS Energy Lett.*, 2021, **6**, 1511-1520.
6. N. Bonanos and F. Willy Poulsen, *J. Mater. Chem.*, 1999, **9**, 431-434.
7. T. Schober, W. Schilling and H. Wenzl, *Solid State Ionics*, 1996, **86-88**, 653-658.
8. C. Duan, J. Huang, N. Sullivan and R. O'Hayre, *Appl. Phys. Rev.*, 2020, **7**, 011314.
9. E. Vollestad, R. Strandbakke, M. Tarach, D. Catalan-Martinez, M. L. Fontaine, D. Beeaff, D. R. Clark, J. M. Serra and T. Norby, *Nat. Mater.*, 2019, **18**, 752-759.
10. L. Jiang, F. Li, T. Wei, R. Zeng and Y. Huang, *Electrochim. Acta*, 2014, **133**, 364-372.
11. S. Li, Z. Lü, X. Huang, B. Wei and W. Su, *Solid State Ionics*, 2007, **178**, 417-422.
12. Z. Li, B. Wei, Z. Lü, X. Huang and W. Su, *Solid State Ionics*, 2012, **207**, 38-43.
13. Y. Wang, F. Jin, X. Hao, B. Niu, P. Lyu and T. He, *J. Alloys Compd.*, 2020, **829**, 154470.
14. C. Duan, J. Tong, M. Shang, S. Nikodemski, M. Sanders, S. Ricote, A. Almansoori and R. O'Hayre, *Science*, 2015, **349**, 1321.
15. H. Ding, W. Wu, C. Jiang, Y. Ding, W. Bian, B. Hu, P. Singh, C. J. Orme, L. Wang, Y. Zhang and D. Ding, *Nat. Commun.*, 2020, **11**, 1907.
16. M. Saqib, I.-G. Choi, H. Bae, K. Park, J.-S. Shin, Y.-D. Kim, J.-I. Lee, M. Jo, Y.-C. Kim, K.-S. Lee, S.-J. Song, E. D. Wachsman and J.-Y. Park, *Energy Environ. Sci.*, 2021, **14**, 2472-2484.
17. K. Park, H. Bae, H. K. Kim, I. G. Choi, M. Jo, G. M. Park, M. Asif, A. Bhardwaj, K. S. Lee, Y. C. Kim, S. J. Song, E. D. Wachsman and J. Y. Park, *Adv. Energy Mater.*, 2022, **13**, 2202999
18. J. Kim, S. Sengodan, G. Kwon, D. Ding, J. Shin, M. Liu and G. Kim, *ChemSusChem*, 2014, **7**, 2811-2815.
19. M. Liang, Y. Zhu, Y. Song, D. Guan, Z. Luo, G. Yang, S. P. Jiang, W. Zhou, R. Ran and Z. Shao, *Adv. Mater.*, 2022, **34**, 2106379.
20. K. Xu, H. Zhang, Y. Xu, F. He, Y. Zhou, Y. Pan, J. Ma, B. Zhao, W. Yuan, Y. Chen and M. Liu, *Adv. Funct. Mater.*, 2022, **32**, 2110998.

21. K. Pei, Y. Zhou, K. Xu, H. Zhang, Y. Ding, B. Zhao, W. Yuan, K. Sasaki, Y. Choi, Y. Chen and M. Liu, *Nat. Commun.*, 2022, **13**, 2207.
22. S. Choi, C. J. Kucharczyk, Y. Liang, X. Zhang, I. Takeuchi, H.-I. Ji and S. M. Haile, *Nat. Energy*, 2018, **3**, 202-210.
23. F. Liu, H. Deng, D. Diercks, P. Kumar, M. H. A. Jabbar, C. Gumeci, Y. Furuya, N. Dale, T. Oku, M. Usuda, P. Kazempoor, L. Fang, D. Chen, B. Liu and C. Duan, *Nat. Energy*, 2023, **8**, 1145-1157.
24. J. H. Kim, D. Kim, S. Ahn, K. J. Kim, S. Jeon, D.-K. Lim, J. K. Kim, U. Kim, H.-N. Im, B. Koo, K. T. Lee and W. Jung, *Energy Environ. Sci.*, 2023, **16**, 3803-3814.
25. F. He, Y. Zhou, T. Hu, Y. Xu, M. Hou, F. Zhu, D. Liu, H. Zhang, K. Xu, M. Liu and Y. Chen, *Adv. Mater.*, 2023, **35**, 2209469.
26. D. Kim, I. Jeong, S. Ahn, S. Oh, H. N. Im, H. Bae, S. J. Song, C. W. Lee, W. Jung and K. T. Lee, *Adv. Energy Mater.*, 2024, **14**, 2304059.
27. M. Choi, D. Kim, T. K. Lee, J. Lee, H. S. Yoo and W. Lee, *Adv. Energy Mater.*, 2024, DOI: 10.1002/aenm.202400124.
28. Y. Dong, C. Chen, M. Liu, B. H. Rainwater and Y. Bai, *Fuel Cells*, 2019, **20**, 70-79.
29. W. Zhang, Y. Zhou, E. Liu, Y. Ding, Z. Luo, T. Li, N. Kane, B. Zhao, Y. Niu, Y. Liu and M. Liu, *Appl. Catal., B: Environ.*, 2021, **299**, 120631.
30. J. Kim, A. Jun, O. Gwon, S. Yoo, M. Liu, J. Shin, T.-H. Lim and G. Kim, *Nano Energy*, 2018, **44**, 121-126.
31. F. Zhu, F. He, D. Liu, H. Zhang, Y. Xu, K. Xu and Y. Chen, *Energy Storage Mater.*, 2022, **53**, 754-762.
32. Y. Xu, K. Xu, F. Zhu, F. He, H. Zhang, C. Fang, Y. Liu, Y. Zhou, Y. Choi and Y. Chen, *ACS Energy Lett.*, 2023, **8**, 4145-4155.
33. M. Hou, F. Zhu, Y. Liu and Y. Chen, *J. Eur. Ceram. Soc.*, 2023, **43**, 6200-6207.
34. G. Li, Y. Gou, R. Ren, C. Xu, J. Qiao, W. Sun, Z. Wang and K. Sun, *J. Power Sources*, 2021, **508**, 230343.